Applied Thermal Engineering 294 (2026) 130662

Contents lists available at ScienceDirect

Applied Thermal Engineering

journal homepage: www.elsevier.com/locate/apthermeng

Research Paper

Experimental characterization of specific heat capacity and dynamic heat generation rate for Lithium-ion battery cells using surface heat flux sensors[☆]

Wei He [a], Hengyun Zhang [a,*], Shen Xu [a], Xinwei Wang [b]

[a] School of Mechanical and Automotive Engineering, Shanghai University of Engineering Science, 333 Longteng Road, Songjiang, Shanghai 201620, China
[b] Department of Mechanical Engineering, 2025 Black Engineering Building, Iowa State University, Ames, IA 50011, USA

ARTICLE INFO

Keywords:
Lithium-ion battery
Specific heat capacity
Instantaneous heat generation rate
Heat flux sensor
Dynamic operating condition

ABSTRACT

Specific heat capacity and heat generation rate (HGR) of lithium-ion batteries (LIBs) are key parameters for thermal management modelling and thermal safety evaluation. This study proposes a measurement method based on surface heat flux sensors (HFSs) that enables instantaneous heat flux acquisition and thus real-time calibration of heat loss and temperature rise. The present method allows the experimental determination of both specific heat capacity of the cell and the instantaneous HGR. Under the constant heating power condition, the specific heat capacity of the cell was measured over a wide temperature range from −5 °C to 55 °C, while HGR behavior was analyzed at different discharge rates. The results showed excellent agreement with those obtained from a calibrated calorimetry method, with maximum deviations of 0.72% and 2.94%. A standard sample test was also conducted and good agreement was achieved. Having validated the method, it was further applied to analyze HGR behavior under the dynamic worldwide harmonized light-duty test cycle (WLTC). By applying the WLTC-derived transient current profile to the cell, the instantaneous temperature rise and surface heat flux were recorded. These measurements yield the time-varying HGR throughout the dynamic cycle in association with vehicle speed. Both exothermic heat during driving and endothermic heat during regenerative braking can be captured using the present measurement method. Peak HGR appears in the high-speed phase near the end of each cycle, whereas the cycle-averaged HGR remains far below the peak value. Our developed method allows both static and dynamic characterization of the battery thermal parameters in a fast manner.

1. Introduction

Driven by the great need of transport electrification and carbon neutrality, lithium-ion batteries (LIBs) have become the predominant energy storage technology for electric vehicles and grid-scale systems due to their high energy density, high power density, and long cycle life. Nonetheless, the safety, performance, and lifespan of LIBs are largely governed by cell temperature and its spatial uniformity [1]. Accurate temperature prediction and thermal management of battery systems rely on reliable thermal parameters. In thermal management modelling and design, specific heat capacity and heat generation rate (HGR) of the cell are the two key parameters that dictate temperature rise and temperature field evolution.

Since temperature serves as a critical state variable in equivalent circuit models and lifetime estimation algorithms, any errors in thermal parameters would lead to temperature estimation errors, which in turn affect the state-of-health (SOH) estimation and remaining useful life prediction, ultimately influencing vehicle-level performance and safety decisions [2]. Specific heat capacity quantifies the temperature increase caused by absorbed heat. Overestimation of specific heat capacity causes the thermal model to underestimate the rate of temperature rise, potentially leading to insufficient cooling capacity and undesired thermal safety issues in electric vehicles, whereas the underestimation, conversely, results in excessive temperature rise and thus increased investment on cooling or pre-heating, and thus reduced remaining energy and driving range [3]. It has been documented that large deviations in specific heat capacity significantly affect the accuracy of thermal runaway propagation prediction in battery packs [4].

Heat generation in LIBs originates from Joule heating and reversible/

[☆] This article is part of a Special issue entitled: ‘ATE_ExHFT-11’ published in Applied Thermal Engineering.

[*] Corresponding author.
E-mail address: zhanghengyun@sues.edu.cn (H. Zhang).

https://doi.org/10.1016/j.applthermaleng.2026.130662
Received 11 January 2026; Received in revised form 5 March 2026; Accepted 16 March 2026

Nomenclature

A, A_f	battery surface area, vehicle frontal area(m^2)
c	specific heat capacity of the battery ($J\cdot kg^{-1}\ {}^{\circ}C^{-1}$)
C_D	drag coefficient
d_1, d_2-d_1, d_{2hf}-d_2,d_3-d_{2hf}	half of the battery width, thicknesses of the film heater, sensor thickness of heat flow, thickness of the insulation material(m)
f	car rolling resistance coefficient
g	gravitational acceleration(m/s^2)
h_{tot}	heat transfer coefficients for convection and radiation, respectively ($W\cdot m^{-2}\ {}^{\circ}C^{-1}$)
I	battery current(A)
k_b, k_{ht}, k_{hfs}, k_{ti}	thermal conductivities of battery, the film heater, the heat flow sensor, the insulation material, respectively ($W\cdot m^{-1}\ {}^{\circ}C\ ^{-1}$)
m,m_{car}	battery mass, car mass(kg)
P_{in},P_b	Heating power supplied to the battery, car output power (W)
Q_{loss}	heat loss (J)
q_{gen},q_{loss},	battery heat generation rate, battery heat loss rate (W)
q''	heat flux (W/m^2)
R_{tot}'', R_b''	specific thermal resistances from the battery to the environment, and from the battery average temperature to its surface temperature (°C /W)
R_{ht}'', R_{hfs}''	specific thermal resistances of heater, and heat flow sensor, respectively (°C /W)
R_{ti}'', $R_{ti,a}''$	specific thermal resistances of the thermal insulation itself and from the thermal insulation to the environmental temperature T_a (°C /W)
S_T	heat flow meter sensitivity ($V/(W/m^2)$)
S_{calib}	calibration coefficient
t_0,t_1,t_2	heating start time, end time of heating, time to reach thermal equilibrium (s)
T_a	environmental temperature (°C)
T,T_{avg}, T_{bo}	thermocouple temperature, battery average temperature, surface temperature (°C)
U	battery voltage (V)
V_a	vehicle speed (m/s)
ΔV	heat flux meter voltage (V)

Greek symbols

η, η_E	Vehicle transmission efficiency, electric conversion efficiency
α	slope angle (°)
δ	rotational mass conversion factor

Acronyms

ARC	Accelerating rate calorimetry
DSC	differential scanning calorimeter
DC	direct current
HGR	heat generation rate (W)
HFS	Heat flux sensor
NBR	nitrile butadiene rubber
NCM	nickel-cobalt-manganese
SOH	state of health
WLTC	Worldwide harmonized light-duty test cycle

irreversible electrochemical reactions. Underestimating HGR leads to under-prediction of peak temperature and temperature gradients, resulting in delayed control response and compromised reliability. An overestimation on the HGR, on the other hand, would introduce unnecessary design redundancy in thermal management and undesired derating in driving power [5].

Therefore, accurate determination of specific heat capacity and HGR, particularly the transient HGR under real-world dynamic driving cycles, constitutes an essential prerequisite for effective thermal management and thermal safety design of LIBs.

Existing methods for measuring the specific heat capacity of LIBs can be broadly classified into two categories, as discussed in recent systematic reviews on experimental determination of thermophysical parameters for lithium-ion batteries [6]. The first category involves weighted averaging of material-level measurements. Loges et al. [7] used differential scanning calorimetry (DSC) to determine the specific heat capacities of electrodes, separator, and electrolyte, and then calculated the full-cell value through mass-weighted averaging. Although this approach offers excellent repeatability, it requires cell disassembly, during which electrolyte evaporation or leakage can introduce significant deviations.

The second category comprises full-cell calorimetry techniques, in which a known heat input or power excitation is applied under controlled ambient conditions, and the specific heat capacity is derived from the energy balance equation. Bryden et al. [8] developed a simplified method using conventional laboratory equipment with a correction in thermal leakage, achieving values comparable to those from commercial calorimeters. Nonetheless, the approach proved sensitive to environmental disturbances. Faber et al. [9] proposed an adiabatic-box method that minimizes uncertainties in environmental heat exchange, thereby enhancing applicability to cells of various form factors. Nevertheless, the results depend on empirical corrections derived from multiple cycles and thus excessively long measurement time. Zhang et al. [10] introduced a calibrated calorimetry technique based on constant-power heating, where the specific heat capacity is calculated from energy balance during heating and cooling phases. This technique eliminates the need for cell disassembly and reduces overall test duration, yet the calibration still requires fitting of radial heat-loss parameters from the slow natural cooling curves [11], which is a slow process preventing rapid acquisition of specific heat capacity.

Specific to conventional calorimetric techniques, efforts have been made on the heat flux sensor (HFS) based approaches to determine the specific capacity of lithium-ion cells, though not many. For instance, Murashko et al. [12] used gradient heat flux sensors to measure the net heat flow and thus simultaneously determine the specific heat capacity of pouch-type cells. More recently, Auch et al. [13] employed an HFS-based experimental approach to measure the specific heat capacity of cylindrical cells through direct acquisition of the heat flux into the cell, demonstrating the feasibility of heat-flux-based calorimetric characterization. In their study, the specific heat capacity was identified using a step temperature rise method, where the heat-loss treatment was inferred from the cooling angle during the transient process.

The instantaneous HGR of a cell is mostly obtained through two different approaches. The first is the electrochemical-thermal coupled method based on the Bernardi equation summing the Joule heat, polarisation heat, and reversible reaction heat (including entropic heat) to determine the HGR, which is then calculated at the full-cell level using pre-measured voltage, current, and entropy coefficient data [14]. Xu et al. [15] identified a systematic amplification effect caused by external leads on heat estimation and proposed a correction for the effect of lead wire. Based on systematic measurements of overpotential and entropy coefficients, they developed a full-factorial surrogate model of heat generation power using depth of discharge, C-rate, and ambient temperature as input variables. Their results highlight the non-negligible role of reversible reaction heat in total heat generation. Under the worldwide harmonized light-duty test cycle (WLTC), the model predicted temperature rise with deviations of approximately 0.8–1.6 °C compared with experiments. Jindal et al. [16] applied the Bernardi equation to both lithium iron phosphate (LFP) cells and nickel-cobalt-manganese (NCM) cells and conducted constant-current continuous discharge and pulse-discharge experiments to compare the model-estimated instantaneous HGR with calorimetric measurements. Their results show that, under steady continuous discharge, the Bernardi-based estimation exhibits small deviations from calorimetric measurements. However, under pulse-discharge conditions, strong voltage fluctuations and limited identification accuracy of the polarisation and entropic terms lead to significant deviation in HGR. As a result, transient heat behavior cannot be accurately captured, which restricts direct application of this method under complex dynamic operating conditions in electric vehicles.

The second approach concerns the calorimetric methods that directly measure heat generation. Hu et al. [17] designed a full-cell calorimetry apparatus based on a thermoelectric cooling control loop, where active temperature control established quasi-isothermal boundary conditions. Using this device, heat-generation curves of large-format lithium-ion cells were obtained under various charge and discharge rates. Although this type of method can capture transient heat-generation behavior, the experimental setup was complex, and temperature fluctuations introduced errors through the control loop required careful static and dynamic calibrations.

Ding et al. [18] used an accelerating rate calorimeter (ARC) to measure the HGR of large-format lithium-ion cells at different C-rates. Their results show that ARC can provide high-sensitivity HGR curves across a wide temperature range. However, ARC operation requires the cell and the chamber to remain in thermal equilibrium, which leads to long test durations. In addition, ARC testing suffers from temperature non-uniformity within the cell and cannot capture endothermic behaviors (negative HGR). It has also been reported that ARC systems are not perfectly adiabatic, and systematic heat loss can introduce additional deviations in heat-generation estimation. He et al. [19] analyzed the heat-transfer characteristics of ARC systems and found that, as cell size increases, the mismatch between internal thermal inertia and chamber heat-exchange conditions amplifies temperature gradients and heat-transfer errors, further increasing the uncertainty in large-format cell measurements [20]. Wu et al. [21] investigated HGR of cylindrical battery cells during discharge using a calibrated calorimetry method. Under thermal insulation conditions, system heat loss was calibrated through constant-power heating, and the corrected energy balance was applied to cell charge–discharge tests to obtain transient HGR curves. Their results demonstrate that this method can accurately reflect the dynamic heat-generation characteristics of cells and reveal the strong increase in HGR with rising C-rate. Validation studies indicate good repeatability and applicability, making calibrated calorimetry suitable for quantitative characterization across operating conditions. Nevertheless, the characterization of HGR under highly dynamic conditions with complex temperature fluctuations such as real-world driving cycles remains limited, which is yet to be examined. In addition, most existing approaches treat specific heat capacity and HGR as separate measurement processes, lack of unified workflow for parameter determination.

To address the above limitations, this study proposes a robust nondestructive full-cell experimental framework based on instantaneous heat flux sensing using the thermoelectric HFS. By coupling real-time surface heat flux acquisition with battery cell temperature rise, the method enables simultaneous identification of specific heat capacity and instantaneous HGR with the same experimental setup. Unlike conventional calibrated calorimetry and HFS techniques, which require either prolonged post-heating cooling for heat loss fitting [22] or cooling angle calibration [13], the present approach could provide a real-time and robust heat-loss correction during the heating process, significantly reducing test duration. The framework is further extended to vehicle-derived dynamic current profiles, allowing direct measurement of transient HGR under WLTC conditions. The uniqueness of this work lies in establishing a unified experimental workflow that integrates surface heat flux sensing and instantaneous heat-loss correction to determine the full-cell specific heat capacity and dynamic HGR characterization within one experimental setup, insensitive to the geometrical configurations. As such, the present study is different from previous HFS-based or calorimetric approaches, which would provide a robust method for efficient and accurate thermal parameters under highly dynamic operating conditions in a fast manner.

2. Experimental method

A commercially available large-format prismatic cell of 54 Ah was used as the test battery. The anode consisted of graphite, and the cathode was composed of lithium iron phosphate. The detailed specifications of the cell are listed in Table 1. In this work, the measurement method was developed by surface-mounting HFSs for determination of both specific heat capacity and HGR of intact lithium-ion battery cells. The experimental methods for specific heat capacity and HGR are presented in Sections 2.1 and 2.2, respectively, while the conversion of the driving cycle to the battery current profile is introduced in Section 2.3. The complete experimental procedure and setup are described in Section 2.4, where the overall schematic of the experimental configuration is also provided as Fig. 3.

2.1. *Method development for specific heat capacity measurement*

In the specific heat capacity measurement, the two large surfaces of the battery were first pasted with a thin film heater of thickness 0.36 mm to supply heating power to the battery. The HFS was then attached to the film heater, and the assembly was finally wrapped around with a layer of thermal insulation made of NBR.

The HFS used in this study is composed of a thermopile formed by multiple thermoelectric arms made of bismuth telluride sandwiched between two polyimide layers. When heat flows normally through the sensor from the cell surface, a minute temperature difference is generated between its upper and lower surfaces. The thermopile converts this temperature difference into a direct-current (DC) voltage output via the Seebeck effect [23]. Owing to the integrated thermopile structure inside the sensor, the output voltage is linearly proportional to the normal heat flux. A larger heat flux produces a larger temperature difference across the plate, and the thermopile converts this difference into a measurable voltage signal representing the normal heat flux [24]. The proportionality constant, defined as the sensitivity S_T, is governed by the equivalent Seebeck coefficient of the thermoelectric material as well as the effective thickness and effective thermal conductivity of the sensor.

In engineering calculations, the heat flux is obtained by converting the measured voltage using the calibrated sensitivity [25]. The sensitivity under standard conditions together with a temperature coefficient or empirical correction function, is expressed as:

$$S_T = [0.00334 \times T + 0.917] \times S_{calib} \tag{1}$$

where S_T is the sensitivity of the HFS at the operating temperature T(°C), S_{calib} is the sensitivity under the reference condition calibrated by the supplier, and the coefficients 0.00334 and 0.917 are temperature-correction parameters provided in the manufacturer's calibration datasheet.

Table 1
Main parameters of the present battery.

Parameter	Value
Cathode	Lithium iron phosphate
Rated capacity	54 Ah
Rated voltage	3.2 V
Total mass	1131.0 g
Dimensions	427 mm × 90 mm × 13.7 mm

With the temperature-corrected sensitivity, the normal heat flux $q''$is calculated as:

$$q'' = \frac{\Delta V}{S_T} \tag{2}$$

where ΔV is the measured output voltage of the HFS.

In the specific heat capacity experiment, the film heater is switched on at t_0 and maintained until t_1, after which the heating is stopped and the cell is naturally cooled to t_2, in order to homogenize the internal temperature non-uniformity of the battery similar to the calibrated calorimetry [26]. During the time interval [t_0, t_2], the heat supplied by the film heater from t_0 to t_1 was divided into two parts: one portion was absorbed by the cell to increase its temperature due to heat capacity and the rest was dissipated to the environment through the thermal insulation layer. The energy conservation equation is thus expressed as:

$$\int_{t_0}^{t_1} P_{in}(t)dt = mc\left[T_{avg}(t_2) - T_{avg}(t_0)\right] + Q_{loss} \tag{3}$$

where $P_{in}(t)$ is the instantaneous heating power, t_0, t_1, and t_2 are the start time of heating, end time of heating, and the time when the thermal equilibrium is reached, respectively, m is the cell mass, c is the specific heat capacity, T_{avg} is the average cell temperature in relation with time, and Q_{loss} is the total heat loss to the surroundings during the entire period. The specific heat capacity is then obtained by rearranging Eq. (3):

$$c = \frac{\int_{t_0}^{t_1} p_{in}(t)dt - Q_{loss}}{m\left[T_{avg}(t_2) - T_{avg}(t_0)\right]} \tag{4}$$

The lost heat is obtained by integrating the heat-dissipation rate over time

$$Q_{\mathrm{loss}} = \int_{t_0}^{t_2} q_{loss}dt \tag{5}$$

where q_{loss} denotes the instantaneous heat dissipation rate (W), whereas Q_{loss} represents the total heat loss (J) integrated over the entire time interval [t_0, t_2]. It should be pointed that the instantaneous determination of the dissipated heat is the key difference between the present HFS-based method and the conventional calibrated calorimetry method. In the calibrated calorimetry approach, the dissipated heat is obtained using the following expression:

$$Q_{\mathrm{loss}} = mc\int_{t_0}^{t_2} L_{cool}dt \tag{6}$$

Here L_{cool} is the heat-loss rate resulting from thermal dissipation during the natural cooling process after t_2, which requires sufficiently long cooling period, normally several hours, to calibrate the heat loss. Differently, the present HFS-based method can obtain the dissipated heat instantaneously and omitting additional prolonged cooling-down step. This fundamental difference between the two approaches provides the basis for the comparative analysis presented later in this study.

In the experiment, multiple HFSs were attached to the cell surface, and the readings from multiple HFSs were averaged to represent the overall heat dissipation over area A. Thus, the heat dissipation flux to the surroundings is as follows:

$$q_{loss}(t) = \frac{A}{n}\sum_{i=1}^{n} q_i''(t) \tag{7}$$

where A is the effective heat-transfer surface area of the cell and n is the number of HFSs.

It is noted that the above expression Eq. (4) provides the specific heat capacity given the ambient temperature. By repeating the experiment at different ambient temperatures, the specific heat capacity of the cell at different temperatures can be obtained.

Fig. 1 shows the physical model of a prismatic battery with the thickness ($2d_1$) and height H. It is covered with a film heater, heat flow sensor and thermal insulation layer at the two large lateral surfaces whereas the other four small surfaces are assumed adiabatic. It should be clarified that the adiabatic assumption is introduced only for method illustration based on the one-dimensional thermal resistance network.

For the tested prismatic cell (427 mm × 90 mm × 13.7 mm), the two large faces (427 × 90 mm^2) account for approximately 84.4% of the total external surface area, whereas the four narrow faces collectively represent only about 15.6%. Taking the specific capacity test at 25 °C for analysis, the total measured heat loss during the specific heat experiment was approximately 7.6% of the total input heating energy. Under the reasonable estimation assuming heat loss is proportional to surface area, the percentage contribution from the four narrow faces would be approximately 7.6% × 15.6% ≈ 1.2% of the total energy input. This indicates that lateral heat leakage is minimal and has negligible influence on the results.

Based on the one-dimensional heat transfer, the specific thermal resistance network at the end of thermal equalization time t_2 can be formulated as follows. The total specific thermal resistance R_{tot}'' is given as follows:

$$\mathrm{R_{tot}}'' = \mathrm{R_b}'' + \mathrm{R_{ht}}'' + \mathrm{R_{hfs}}'' + \mathrm{R_{ti}}'' + \mathrm{R_{ti,a}}'' \tag{8}$$

$$\mathrm{R_b}'' = \frac{\mathrm{d_1}}{4\mathrm{k_b}} \tag{9}$$

$$\mathrm{R}_{ht}'' = \frac{\mathrm{d_2 - d_1}}{\mathrm{k_{ht}}} \tag{10}$$

$$\mathrm{R}_{hfs}'' = \frac{\mathrm{d_{2hf} - d_2}}{\mathrm{k}_{hfs}} \tag{11}$$

$$\mathrm{R_{ti}}'' = \frac{\mathrm{d_3 - d_2}}{\mathrm{k_{ti}}} \tag{12}$$

$$\mathrm{R_{ti,a}}'' = \frac{1}{\mathrm{h_{tot}}} \tag{13}$$

where R_{tot}'' is the overall resistance from the battery to the environment, R_b'' is the specific thermal resistance from the battery average temperature T_{avg} to its surface temperature T_{bo}, R_{ht}'' is the specific thermal resistance of heater, R_{hfs}'' is the specific thermal resistance across the heat flow sensor, R_{ti}'' is the specific thermal resistance of the thermal insulation, $R_{ti,a}''$ is the specific thermal resistance from the thermal insulation to the environmental temperature T_a, d_1 is half of the battery width, (d_2-d_1) is the thickness of the film heater, and ($d_{2\mathrm{hf}}$-d_2) is the heat flow sensor thickness, (d_3-$d_{2\mathrm{hf}}$) is the thickness of the insulation material. k_b, k_{ht}, k_{hfs} and k_{ti} represent the thermal conductivities of the battery in the normal direction, the film heater, the HFS and the insulation material, respectively. Note that the heat transfer coefficient h_{tot} in Eq. (10) combines both convective heat transfer and radiative heat transfer effects, which is determined to be 12.1 $\mathrm{W{\cdot}m^{-2^{\circ}C-1}}$ [26] at a typical temperature difference of 25 °C. It should be noted that the insertion of HFS in place of the insulation in Fig. 1(a) has only a minimal effect on the overall thermal resistance. Our calculation shows that the HFS thermal resistance amounts to only 0.29% of the overall cell thermal resistance with aerogel as insulation and 0.49% with NBR as insulation. Thus, the effect of adding HFS on the heat flow measurement could be ignored in the following characterization of the battery thermal parameters. In addition, based on the established one-dimensional thermal resistance network, the Biot number was evaluated using

$$Bi = \frac{d_1}{k_{\mathrm{b}}\left(R_{\mathrm{ht}}'' + R_{\mathrm{hfs}}'' + R_{\mathrm{ti}}'' + R_{\mathrm{ti,a}}''\right)} \tag{14}$$

The calculated Biot number is 0.016, which is far less than unity. This

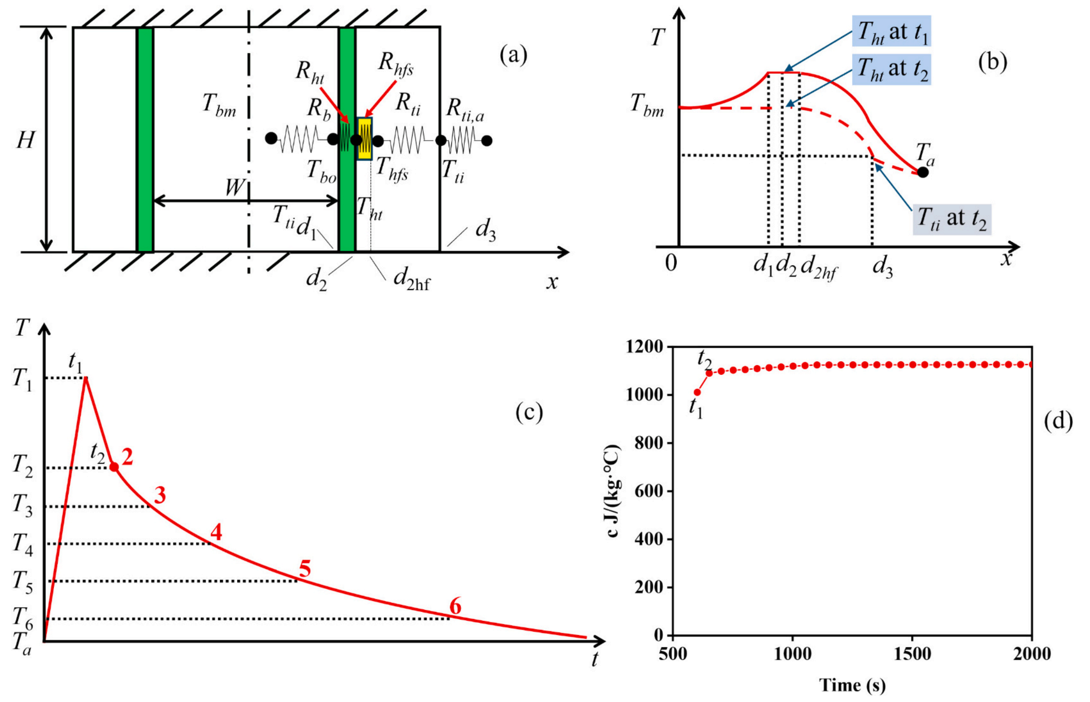

Fig. 1. One-dimensional theoretical model: (a) Thermal resistance network (not to scale), (b) Temperature distributions at t_1 and t_2 for the different components not to the scale, (c) Battery temperature evolution,(d) Specific heat capacity obtained over different time windows.

further confirms that the battery cell can be treated as a lumped thermal mass, and its internal temperature distribution can be regarded as approximately uniform [27].

Fig. 1(d) examplifies the variation of the specific heat capacity identified by the HFS method as the function of the cooling time at an ambient temperature of 25 °C. It can be observed that the identified specific heat capacity gradually converges to a stable value of approximately 1125 J·kg^{-1}·°C^{-1} at about 1100s. Upon stopping the heating at 602 s, a certain time period is required for the cell to uniformize its internal cell temperature field, which can be sensed with the surface mounted thermocouples and HFSs. Such a test time may take 300–500 s as exemplified in Fig. 1(d), which is time-efficient in comparison with several more hours as required in the conventional calorimetric methods [26].

2.2. Method development for HGR measurement

In the HGR measurement, the thermocouples are directly mounted on the battery to start the charge/discharge without applying the heating film. The discharge/charge process leads to the battery cell temperature evolution involving both the internal HGR and heat dissipation rate to the surroundings. Accordingly, the instantaneous energy balance equation can be written as:

$$q_{gen}(t) = q_{loss}(t) + mc\frac{dT_{avg}}{dt} \tag{15}$$

where q_{gen} is the HGR and q_{loss} is the heat dissipation rate. The measured specific heat capacity in Section 2.1 can be used. It should be noted that the HGRs under both constant current and dynamic vehicular current load conditions can be tested due to the instantaneous sensing of the HFS. A detailed uncertainty analysis, including the error propagation from the specific heat capacity measurement to the HGR, is presented in Section 4.2.

2.3. Conversion of driving cycle speed to battery current profile

To investigate the dynamic thermal characteristics of automotive power cells, the vehicle speed profile should be converted into the corresponding cell load-current profile, enabling accurate analysis of the thermal response under real driving conditions. According to vehicle dynamics theory [28], the power demand of a vehicle during operation is determined jointly by rolling resistance, gradient resistance, air resistance, and acceleration resistance. The energy balance equation is expressed as:

$$P_b = \frac{1}{\eta\eta_E}\left[\frac{v_a m_{car} g f cos\alpha}{3600} + \frac{v_a m_{car} g sin\alpha}{3600} + \frac{C_D A_f v_a^3}{76140} + \frac{\delta m_{car} v_a}{3600}\frac{dv_a}{dt}\right] \tag{16}$$

where P_b is the instantaneous battery power demand (positive for discharge, negative for regenerative braking), η and η_E are the transmission and electric conversion efficiencies, respectively, V_a is the vehicle speed, m_{car} is the vehicle mass, g is gravitational acceleration, f is the rolling resistance coefficient, α is the slope angle, C_D is the aerodynamic drag coefficient, A_f is the frontal area, and δ is the rotational mass coefficient. dv/dt is vehicle acceleration. The detailed vehicle parameters are exemplified in Appendix A.

Under dynamic operating conditions, the cell terminal voltage exhibits slight temporal fluctuations. The measured voltage over the WLTC driving cycle is shown in the voltage trace in Fig. 2. Since the voltage flucturation is within approximately 0.032 V corresponding to a relative deviation within 1%, the cell terminal voltage can be regarded as constant during a single driving-cycle operation.

Using the average terminal voltage in the single driving-cycle, we can estimate the current from driving power demand as follows:

$$I = \frac{1}{U\eta\eta_E}\left[\frac{v_a m_{car} g f cos\alpha}{3600} + \frac{v_a m_{car} g sin\alpha}{3600} + \frac{C_D A_f v_a^3}{76140} + \frac{\delta m_{car} v_a}{3600}\frac{dv_a}{dt}\right] \tag{17}$$

where I is cell current under dynamic operating conditions, and U is the cell terminal voltage during the driving-cycle operation.

Based on the above equation, the vehicle speed profile can be converted into the corresponding cell current profile using Eq. (17), as

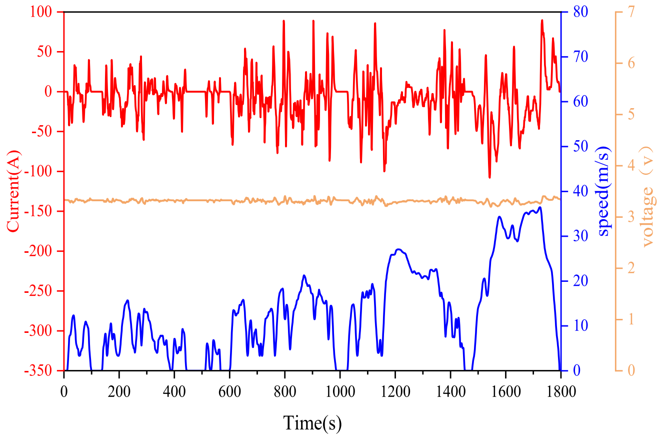

Fig. 2. WLTC driving-cycle speed profile and the corresponding battery current and terminal voltage profiles.

shown in Fig. 2. Since the vehicle speed exhibits pronounced fluctuations over time, and the resulting current profile also fluctuates dynamically, with the current rising rapidly during acceleration, and turning negative during deceleration or braking. Clearly the dynamic vehicle characteristics results in the highly fluctuating current profiles of the cell, which may bring challenges in the characterization of heat generations and thus is to be addressed in the subsequent analysis of this paper.

2.4. Experimental setup and procedure

The HFS-based full-cell measurement was implemented for both the specific heat capacity and the HGR. Fig. 3 illustrates the overall experimental workflow for specific heat capacity and HGR measurements, including the temperature-controlled environment, the flexible heating films, the power-control system, HFSs, the temperature acquisition module, and the data acquisition and analysis platform. The left side corresponds to the specific heat capacity measurement procedure, and the right side corresponds to the HGR measurement procedure. Both experimental tests share the same temperature-control system and data-acquisition platform.

During the specific heat capacity measurement, flexible heating films were attached to both large surfaces of the cell, covering nearly the entire area. Four HFSs were then mounted at the following array locations: upper left, center, and lower right on the front surface, and one-quarter height on the rear surface in dashed line, as shown in Fig. 4. The normal direction and polarity were verified according to the supplier's data. A thin layer of thermal grease was applied between the cell and each HFS to minimize contact thermal resistance and improve measurement accuracy.

In addition, ten K-type thermocouples were arranged along diagonal lines on both surfaces of the cell to characterize the temperature rise by the cell. The thermocouple locations on the front surface are named as upper left, upper 1/4 location, center, lower 1/4 location and lower right, respectively in Fig. 4. After completing all attachments, the cell assembly was encapsulated with NBR. All the wirings, including heater leads, HFS signal lines, and thermocouple wires, were fixed along the edges of the cell to avoid blocking the active sensing area of the HFSs.

The heating films were connected in series to a programmable DC power supply. The millivolt-level differential outputs of the HFSs and all thermocouples were connected to a multi-channel data acquisition system (DAQ), in which differential voltage measurement was employed. The voltage measurement uncertainty of the DAQ was conservatively estimated as approximately ±0.1% of the reading, based on the manufacturer specification and considering additional practical uncertainties in the measurement chain. The DAQ and the DC power supply were controlled by the same computer, which served as the unified master clock. Data acquisition and power output were triggered simultaneously by a single command, ensuring that power, heat flux, and temperature signals were recorded synchronously. The instantaneous voltage and current of the DC power supply were also recorded for subsequent data processing.

The assembled cell was then placed in a temperature-controlled environment chamber. After setting the target ambient temperature (−5, 10, 25, 40, 55 °C), the system was allowed to rest until thermal equilibrium was reached. Equilibrium was determined when the difference between the cell's average temperature and the chamber temperature was less than 0.5 °C and remained within this bound for at least five minutes. This procedure minimized uncertainty in the initial conditions for specific heat capacity identification.

Once the cell average temperature and the ambient temperature had stabilized, a constant heating power was applied. As heating continued, the cell temperature increased and the HFSs recorded the corresponding surface heat dissipation. When the preset temperature rise such as 15 °C was reached at time t_1, heating was stopped. The cell then entered a natural cooling phase to minimize the internal temperature non-uniformity [29]. The test was completed when the temperature

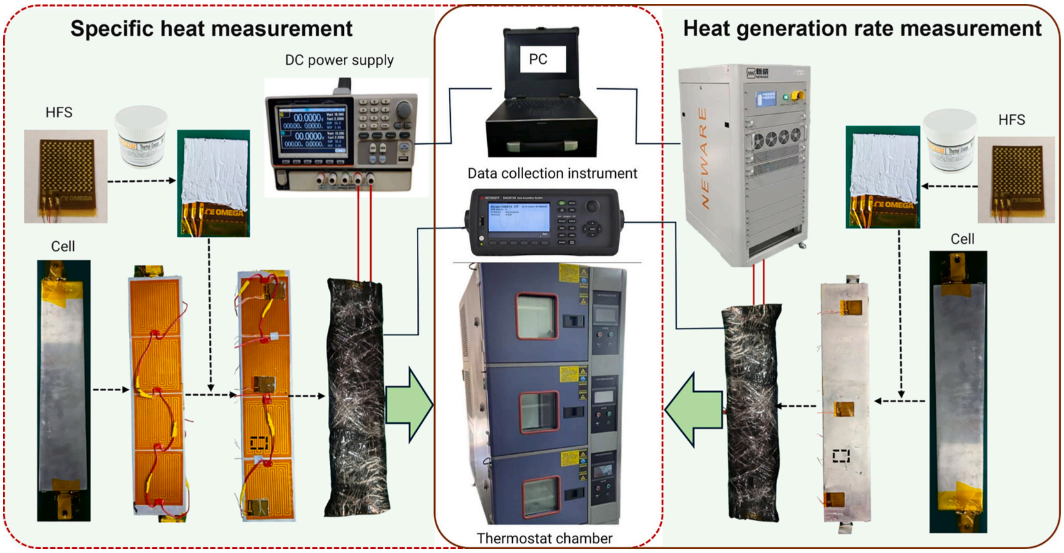

Fig. 3. Experimental setup with the assembly of test cell for the heat capacity and HGR.

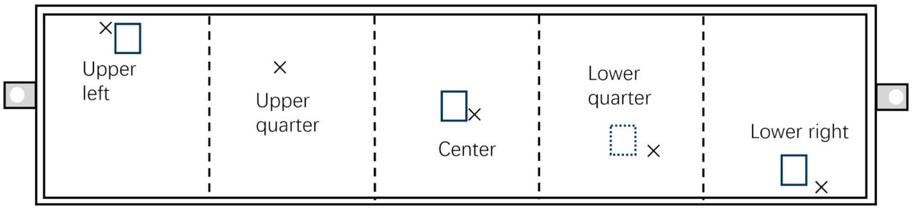

Fig. 4. Locations of three HFSs on the front surface of the battery and one more HFS in dotted line on the rear surface of the battery.

declined to the equilibrium at time t_2, typically within 500 s.

The HGR measurement followed a procedure similar to that used for specific heat capacity test. The HFSs and T-type thermocouples were attached at the same locations of the cell, which was wrapped with insulation and placed in the temperature-controlled environmental chamber and allowed to equilibrate. Cell current, voltage, temperature, and heat flux signals were synchronously recorded by the same DAQ system as has been shown in Fig. 3. The cell was subjected only to discharge conditions imposed by the battery cyclist, so all the heat generation originated from internal Joule and polarisation processes. The experiment was considered complete when the discharge voltage went below the preset threshold voltage. It should be noted that, taking the 1C HGR test of the 54 Ah cell as an example, the calibrated calorimetry method still requires an additional natural cooling period of several hours [26] after the end of discharge to determine the cooling rate, whereas the present HFS-based method can provide the instantaneous HGR immediately at the end of discharge without any extra waiting time.

The complete workflow for determining specific heat capacity and HGR has been implemented in a computer acquisition software system developed in house. The flow chart for the software algorithm is illustrated in Fig. 5.

3. Results and discussion

3.1. Effect of HFS placement

This section evaluates the influence of HFS placements for the test at the full-cell scale. Both the specific heat capacity test and 1C-rate discharge test at the ambient temperature of 25 °C were conducted for illustration.

For each condition, the heat flux measured by each of the four HFSs was compared with the arithmetic average of the four locations. The deviation of each single-point measurement from the surface-averaged heat flux was quantified using the root-mean-square error (RMSE).

$$RMSE = \sqrt{\frac{1}{N}\sum_{K=1}^{N}\left(q_i^{''}(t_k)\text{-}\overline{q}^{''}(t_k)\right)^2} \tag{18}$$

The heat flux and the RMSE deviation of each HFS during the specific heat capacity test are shown in Fig. 6(a) and (b). The RMSE deviation at the lower quarter-location HFS was 0.266 W·m^{-2}, which is much smaller in comparison with the upper-left HFS (2.130 W·m^{-2}), the lower-right HFS (1.917 W·m^{-2}), and the center HFS (3.781 W·m^{-2}). In other words, the heat flux at the lower quarter location most closely matched the surface-averaged heat flux, and the residual band at this location was the narrowest among all the locations.

The heat flux and the RMSE deviation of each single HFS location during the HGR test are shown in Fig. 7(a) and (b), respectively. The RMSE deviation at the quarter-location was 0.375 W·m^{-2}, representing reductions of 77.5% relative to the upper-left location (1.665 W·m^{-2}), 68.8% relative to the lower-right location (1.201 W·m^{-2}), and 84.9% relative to the center location (2.491 W·m^{-2}). Although the test conditions are different, the spatial deviation pattern of the single HFS locations remained nearly identical, for which the center location showed the largest RMSE deviation, and the quarter-location showed the smallest.

These results showed that the quarter-location HFS provided a heat flux most closely representing the surface-averaged heat flux, which is suitable for estimating the overall heat loss of the cell, Q_{loss}. Since the cost of HFSs is non-trivial, the number of HFSs can be reduced by retaining only the lower quarter sensor without causing a noticeable loss of accuracy in engineering applications. In the following sections, the specific heat capacity and HGR calculated using the average heat flux and using only the quarter-location heat flux are further compared to quantifying the resulting deviations.

3.2. Specific heat capacity results and temperature dependence

Specific heat capacity measurements were conducted at ambient temperatures ranging from −5 °C to 55 °C, covering the typical climatic

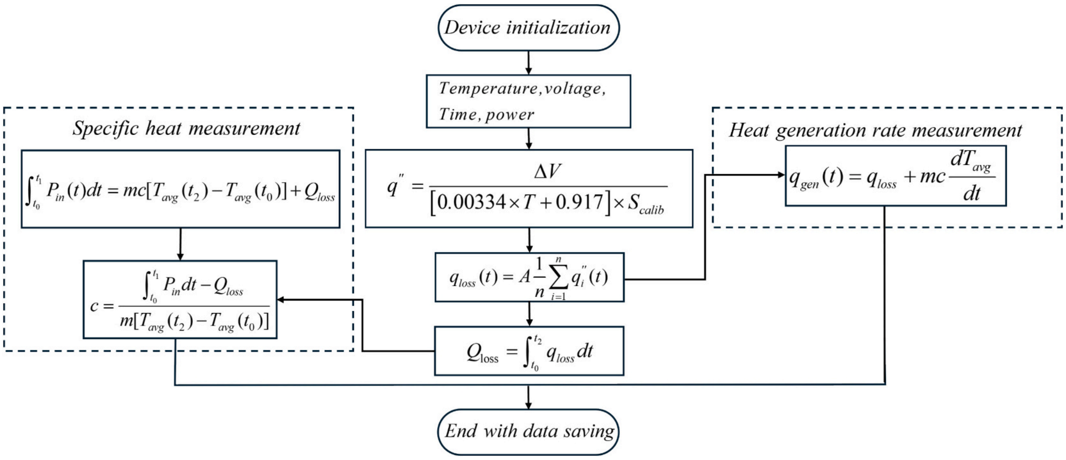

Fig. 5. Flowchart of the unified measurement method for specific heat capacity and HGR based on surface heat flux sensors.

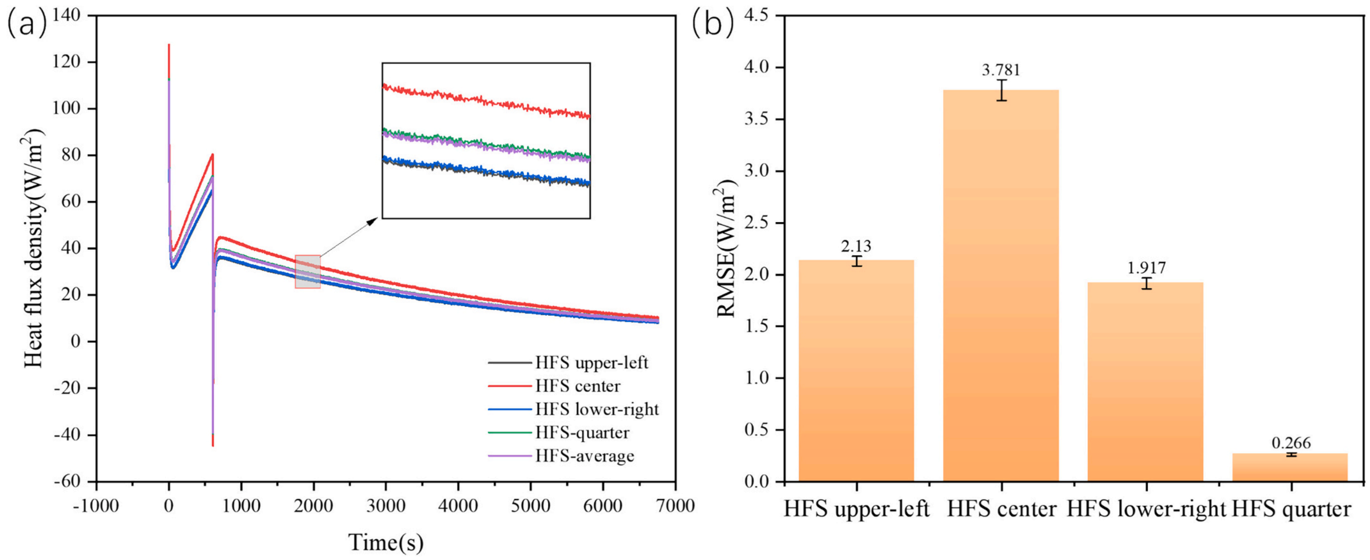

Fig. 6. (a) Heat flux measured during the specific heat capacity test; (b) deviation of the heat flux at each location relative to the surface-averaged heat flux.

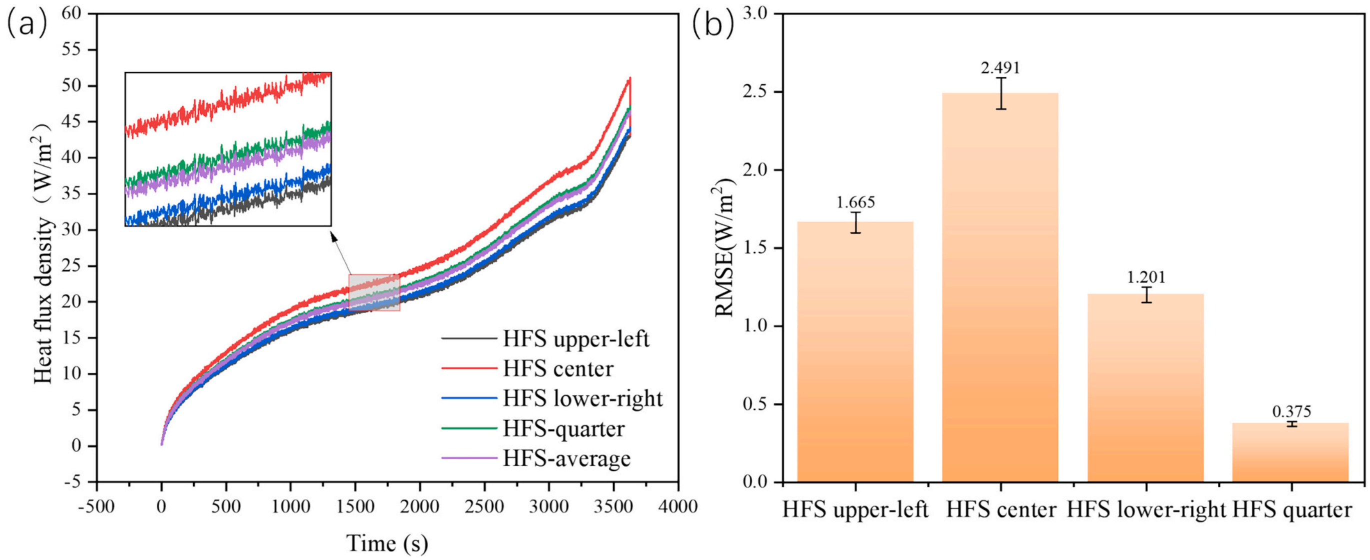

Fig. 7. (a) Heat flux measured during the HGR test; (b) deviation of the heat flux at each location relative to the surface-averaged heat flux.

conditions of the Yangtze River Delta region [30] based on the following two HFS methods by using the arithmetic average of the four-sensor heat fluxes as the surface-averaged heat flux, and using only the heat flux at the quarter-location. In addition, the calibration calorimetry was also conducted for comparison with the HFS method.

The measured results are shown in Fig. 8(a). Fig. 8(b) shows the percentage deviation of the HFS method relative to calibration calorimetry. The relative deviations between the specific heat capacity values obtained by the averaged HFS measurements and those measured by the calibration calorimetry method at ambient temperatures of −5, 10, 25, 40, and 55 °C are +0.72%, +0.63%, −0.25%, +0.64%, and −0.25%, respectively. The corresponding relative deviations of the specific heat capacity values obtained using the quarter-location HFS are +0.50%, +0.31%, −0.59%, +0.28%, and − 0.40%, respectively. Thus the HFS-based method provides accurate and stable measurements of the specific heat capacity in agreement with the calibration calorimeter.

The first-order linear function was used to fit the three data sets. The resulting empirical correlations between specific heat capacity and temperature are given as follows.

$$\begin{array}{ll} \text{Calibration Calorimetry :} & c(T) = 1067.16 + 2.028T, R^2 = 0.980 \\ \text{HFS-avg :} & c(T) = 1073.76 + 1.892T, R^2 = 0.970 \\ \text{HFS-Quarter :} & c(T) = 1070.60 + 1.894T, R^2 = 0.974 \end{array} \tag{19}$$

In summary, the specific heat capacities obtained from the two HFS-based implementations showed the average relative deviations below 0.5% within the temperature range of −5 to 55 °C, and the maximum deviation from the result of the calibration calorimetry method remained below 0.72%. The agreement in both magnitude and temperature dependence demonstrates that the HFS method provides reliable and consistent specific heat capacity measurements. The linear relationships obtained from the present study can be used as inputs for subsequent thermal modelling and engineering estimation.

3.3. HGR results and discharge rate dependence

To elucidate the time-varying characteristics of the cell HGR, the instantaneous HGR profiles under different discharge rates were plotted

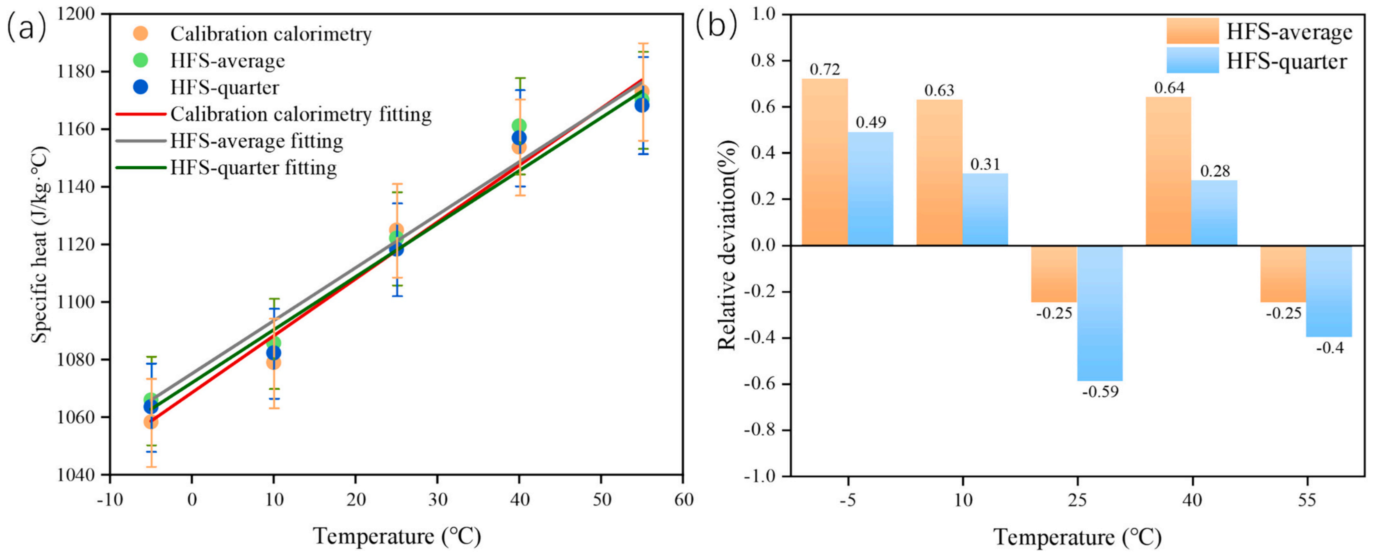

Fig. 8. Specific heat capacity measured at different temperatures and the corresponding deviations compared with the calibration caloriometry: (a) Specific heat capacity measured at different temperatures (b) percentage deviations of the HFS-based results relative to the calibration calorimetry method.

as functions of time, as shown in Fig. 9.

As shown in Fig. 9, the overall level of the cell HGR increases with discharge rate, and the profiles exhibit clear time-varying behavior throughout the discharge process. At lower discharge rates such as 0.5C, the HGR remains at a relatively low level, varying with the discharge time. At higher rates such as 1.5C, the HGR not only increases substantially in magnitude but also exhibits a more pronounced upward trend near the end of discharge.

The time averaged heat generation rates are shown in Fig. 10, as against the results from the calibration calorimetry. In general, the values using the two HFS-based approaches agree within 2% with the calibration calorimetry results except for the 1C test with the relative deviations of 2.94% for the HFS-average method and 3.21% for the HFS-quarter method. The fitted correlations for the avreage heat generation rates are given as follows.

$$\begin{aligned} &\mathit{Calibration\ \ calorimetry}: P(C) = 13.7839C^2 - 2.3789C, R^2 = 0.9994 \\ &\mathit{HFS-avg}: \quad P(C) = 13.9029C^2 - 2.4476C, R^2 = 0.9971 \\ &\mathit{HFS-Quarter}: \quad P(C) = 13.9316C^2 - 2.4426C, R^2 = 0.9971 \end{aligned} \tag{20}$$

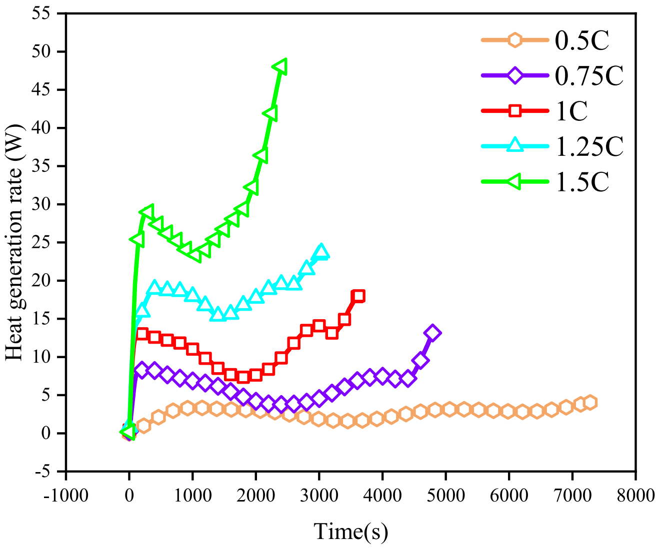

Fig. 9. Time-varying HGR of the cell under different discharge rates.

The fitted results show that the quadratic term is dominant, reflecting the major contribution of Joule heat generation. The linear term provides a slight correction at medium-to-high C-rates, which is associated with polarisation and entropic heat generation [31]. Taken together, the results demonstrate that the HFS-based method and the calibration calorimetry method were highly consistent not only in the magnitude and discharge rate dependence of HGR but also in capturing the detailed time-varying heat-generation behavior.

3.4. Battery thermal behavior under dynamic operating condition

This section extends the present method to the measurement of heat generation behavior under dynamic driving conditions. Based on the speed-current conversion model developed in Section 2, the thermal response of the cell was evaluated under the WLTC.

During the experiment, the cell was fully charged and placed in a thermostatic chamber at an ambient temperature of 25 °C, and then subjected to repeated WLTC cycles until the cut-off voltage was reached. Each WLTC cycle lasted approximately 1800 s, and the total test time was 27,767 s, corresponding to roughly 15 consecutive WLTC cycles with alternating charging and discharging stages. Throughout the test, the cell voltage, current, temperature rise, temperature-change power, heat-loss rate, and total HGR were continuously recorded. In the WLTC dynamic tests, the total HGR was determined from the arithmetic average of the four HFSs mounted on the cell surface.

Fig. 11(a) presents the current and temperature evolution of the cell during WLTC cycling. Each WLTC cycle is separated with two vertical dashed lines. Within each cycle, the current exhibited pronounced peaks and valleys associated with the acceleration, cruising, and braking phases of vehicle operation. The cell temperature showed an overall upward trend, increasing slowly from 25.16 °C to 34.63 °C. Notably, the temperature peak of each cycle occurred shortly after the maximum-speed moment just before the end of the cycle, indicating that heat generation exceeded heat loss near the end of each cycle. After a few cycles, the temperature at the start of the subsequent cycle dropped slightly since the low speed driving in the city drive mode may generate a heat generation rate lower than the heat dissipation rate which increases with temperature. This behavior reflects the typical transient thermal response of the cell under dynamic cycling [32], producing different temperature trajectories in different cycles.

Fig. 11(b) illustrates the full-time evolution of temperature-change power, heat-loss rate, and total HGR. The temperature-change power

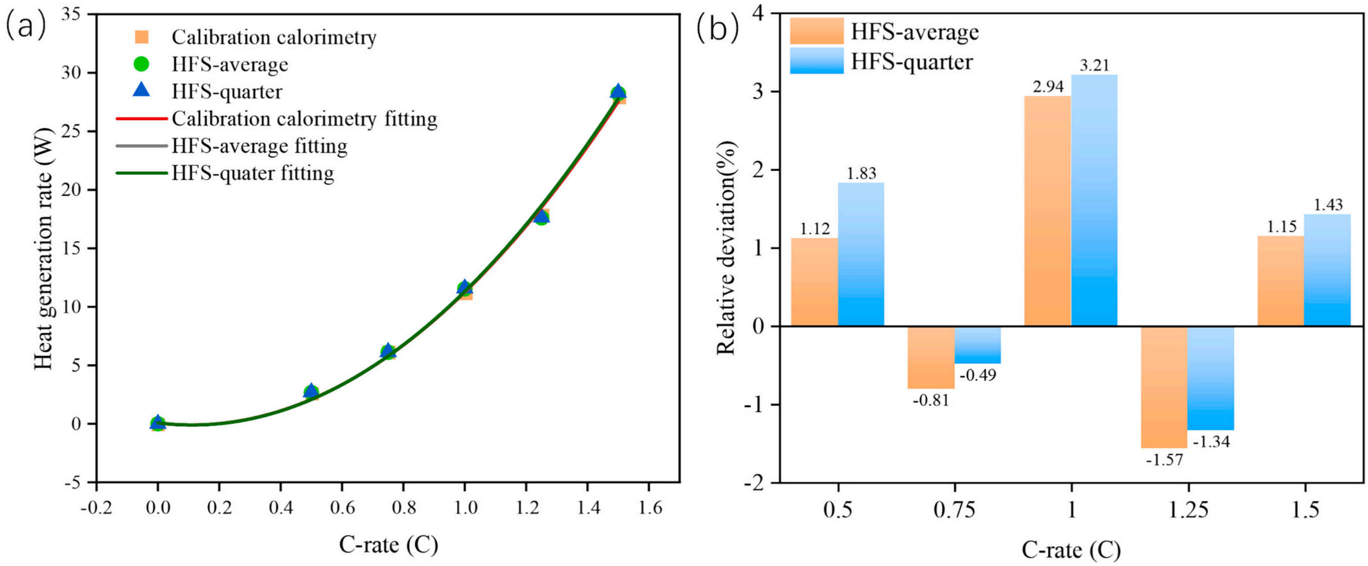

Fig. 10. HGR measured at different discharge rates and the corresponding deviations: (a) HGR measured at different discharge rates (b) percentage deviations of the HFS-based results, using different sensor selections, relative to the calibration calorimetry method.

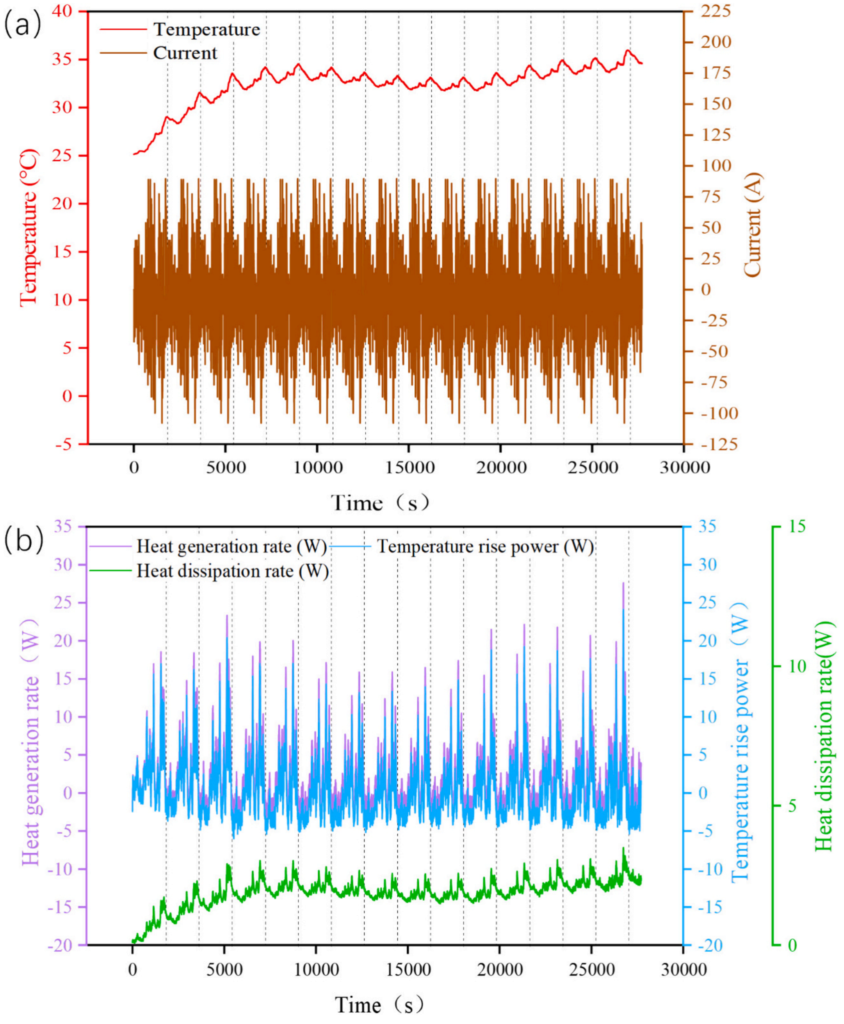

Fig. 11. (a) Cell current and temperature evolution under the WLTC dynamic cycle; (b) instantaneous heat-loss rate, temperature-change power, and HGR over the full cycle.

displayed dense narrow pulses at load-fluctuation events, with peaks of approximately 25–30 W and valleys reaching the negative values −5 W. In comparison, the heat-loss rate first increased as the cell temperature rose and then ocilllated between 1 W and 3 W. The total HGR, obtained as the sum of the two, was synchronised with the current profile. The instantaneous heat generation rose correspondingly as the current surged, whereas heat generation dropped rapidly as the current decreased, which can be mainly attributed to interaction of the Joule heating and entropic heat generation during the highly dynamic cycle. During certain deceleration condition, the discharge changes to charge due to regenerative braking and even transient negative HGR could be obtained. The transient negative heat generation behavior is not a measurement artefact but the result from the dominance of the reversible entropic heat under low current charging conditions. In such cases, the negative entropic heat could exceed the Joule-heating, causing negative heat dissipation and apparently transient heat absorption [33,34].

To further reveal the transient characteristics of the cell HGR under the WLTC dynamic cycle, the WLTC current profile was compared with an equivalent constant-current discharge condition. Since Joule heating accounts for the dominant portion of the total heat generation in most of dynamic operation, and the reversible entropic heat could be partially cancelled with the positive and negative current pulses [35], the following root-mean-square current I_{RMS} could be porposed as the equivalent constant discharge current during dynamic operation. The expression for I_{RMS} is given by:

$$I_{RMS} = \sqrt{\frac{1}{n}\sum_{k=1}^{n} {I_K}^2} \tag{21}$$

The equivalent discharge current under the WLTC cycle was calculated to be 28.3 A, corresponding to a discharge rate of 0.52C. Substituting this rate into the previously established discharge rate-HGR relation yielded an average HGR of 2.48 W. This value differed by only 6.5% from the average HGR of 2.32 W obtained directly from the present HFS measurements, indicating strong consistency between the heat generation under the dynamic cycle and that predicted by the equivalent constant-current discharge.

4. Method validation and uncertainty analysis

4.1. Validation using a standard reference sample

To further verify the accuracy of the HFS-based specific heat capacity measurement method proposed in this study, 304 stainless steel was used for standard sample test. The specimen was a 304 stainless steel block of 2.43 kg with dimensions of 145.44 mm × 26.63 mm × 90.67 mm. A flexible surface-mounted heating film was used to deliver a constant power of 39.2 W for heating, and six thermocouples four HFSs were attached to the sample surface simmilar to the real cell for heat flux acquisition. The measured value was approximately 502 $\mathrm{J{\cdot}kg^{-1}{\cdot}{^\circ}C^{-1}}$, as shown in Fig. 12. which differed by less than 1% from the literature value of 500 $\mathrm{J{\cdot}kg^{-1}{\cdot}{^\circ}C^{-1}}$ [36]. This result demonstrates that the proposed method provides high measurement accuracy.

4.2. Uncertainty analysis of specific heat capacity and HGR

The measurement equipment used in this study included an Agilent 34,972 data acquisition instrument, surface-mounted HFSs, T-type thermocouples, and a DC power supply/battery testing system. Based on the equipment specifications and calibration records, the uncertainty estimates are as follows:

The voltage measurement uncertainty of the Keysight data acquisition instrument was conservatively estimated as approximately 0.1%, based on the manufacturer specification [37] and the voltage and current uncertainties of the DC power supply/testing system are each about 0.1%. The uncertainty of the HFS sensitivity/calibration coefficient S is 2.0% (according to supplier data). The effective area of the HFS has an uncertainty of 0.5%. The T-type thermocouple reading uncertainty is 0.2 °C, which corresponds to about 2% relative uncertainty for a 10 °C temperature rise. The mass of the cell has an uncertainty of about 0.1%.

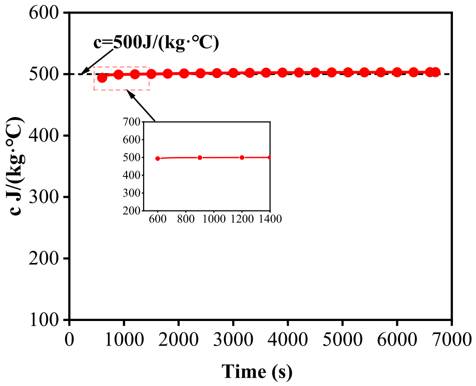

Fig. 12. Specific heat capacity of stainless steel obtained over different time windows.

According to the error propagation method [38], the overall uncertainty of the results is determined by the root-sum-of-squares of the standard uncertainties of the input variables. The uncertainties for the specific heat capacity and the HGR of the cell are estimated using the following equation.

$$\frac{\Delta P_{in}}{P_{in}} = \sqrt{\left(\frac{\Delta U}{U}\right)^2 + \left(\frac{\Delta I}{I}\right)^2} \tag{22}$$

$$\frac{\Delta c}{c} = \sqrt{\left(\frac{\Delta P}{P}\right)^2 + \left(\frac{\Delta S}{S}\right)^2 + \left(\frac{\Delta A}{A}\right)^2 + \left(\frac{\Delta m}{m}\right)^2 + \left(\frac{\Delta T}{T}\right)^2} \tag{23}$$

$$\frac{\Delta q_{gen}}{q_{gen}} = \sqrt{\left(\frac{\Delta c}{c}\right)^2 + \left(\frac{\Delta S}{S}\right)^2 + \left(\frac{\Delta A}{A}\right)^2 + \left(\frac{\Delta m}{m}\right)^2 + \left(\frac{\Delta T}{T}\right)^2} \tag{24}$$

According to Eq. (22), the relative uncertainty of the input power derived from the combined voltage and current is 0.141%. Substituting into Eq. (23) and using the single-quantity uncertainties specified in this study, the uncertainty in the specific heat capacity measured by the HFS method is found to be 2.88%. Similarly, from Eq. (24), the uncertainty in the HGR measured by the HFS method is determined to be 4.07%. Overall, under the experimental conditions of this study, the combined uncertainties for the cell's specific heat capacity and HGR are each controlled within 5%, meeting the requirements for engineering evaluation and method validation [39].

5. Conclusions

In this paper, measurement methods based on surface heat flux sensors were developed to measure the specific heat capacity and HGR of lithium-ion battery cells under different conditions and further extended the method to dynamic driving cycles. A complete HFS-based methodology for determining cell-level thermal parameters was established and cross-validated using the existing calibration calorimetry method. The main conclusions are as follows:

(1) A spatial representativeness analysis was conducted to evaluate the influence of different HFS attachment locations on specific heat capacity and HGR measurements. In comparison with the averages based all the heat flux sensor locations, the relative deviation in RMSE at the quarter-location was only 0.1% (0.27 $\mathrm{W{\cdot}m^{-2}}$ in magnitude), significantly lower than those at the upper-left, center, and lower-right locations, and the

corresponding deviations in the computed specific heat capacity was −0.34%. Under 1C discharge condition at 25 °C, the RMSE at the quarter-location was 0.38 $W\cdot m^{-2}$, again distinctly smaller than those at the upper-left (1.67 $W\cdot m^{-2}$), center (2.49 $W\cdot m^{-2}$), and lower-right (1.20 $W\cdot m^{-2}$) locations, with the lowest heat-generation-rate deviation from the average of all the HFSs. This indicates that a single HFS at the quarter-location could be used without noticeable compromise in accuracy.

(2) The temperature dependence of the cell-level specific heat capacity was investigated across a broad range from −5 °C to 55 °C. Results obtained using both the HFS method and calibration calorimetry show that c increases approximately linearly with temperature. Relative deviations between HFS-based measurements and calibration calorimetry remained ≤1% for both the four-sensor average and the quarter-location method.

(3) The dependence of HGR on discharge rate was characterized in the range 0.5C-1.5C at 25 °C, which can be fitted as quadratic correlation with good fitting of $R^2 > 0.997$ for both HFS-based measurements and calibration calorimetry. In comparison with the conventional calibration calorimetry requiring several hours, the the HFS method could be accomplished in the range of 1000s with the average deviations of less than 1.66% for both the four-sensor average and the quarter-location measurement. The strong agreement confirms the capability of the present method to capture both the magnitude and the discharge rate trend of heat generation.

(4) The applicability of the HFS method under dynamic driving conditions was demonstrated using the WLTC cycle. For the WLTC operations involving approximately 15 alternating charge–discharge cycles, the HGR remained at several watts during low-speed, low-load stages but increased to 20–30 W during high-speed stages immediately before the end of each cycle. The cycle-averaged heat generation power was substantially lower than the instantaneous peak values and closely matched the HGR corresponding to the RMS current. These results quantitatively characterize the transient thermal behavior of lithium-ion batteries under realistic dynamic operating conditions.

It should be noted that different battery types might have different optimal placement of the HFS. As such multi-point temperature or heat flux measurements, or thermal imaging using a thermograph, are recommended to identify the representative location between the maximum and minimum temperature/heat flux in the same principle as reported in this paper.

Beyond the present experimental study, the proposed HFS-based methodology provides a direct experimental support for improving battery thermal modelling and thermal management design. The experimentally determined specific heat capacity and instantaneous HGR can serve as reliable physical inputs for the thermal analysis of practical battery modules and packs, thereby improving temperature prediction accuracy under practical dynamic operating conditions. In particular, the present study faciliates modelling and prediction of vehicle-level thermal management performances under realistic driving cycles, allowing real-time thermal diagnostics and adaptive thermal control systems for advanced electric vehicles.

Declaration of competing interest

The authors declare that they have no known competing financial interests or personal relationships that could have appeared to influence the work reported in this paper.

Acknowledgement

This work was supported by the National Natural Science Foundation of China (52476079).

Appendix A

Table A1
Vehicle parameters used for converting the WLTC speed profile to the current profile.

Parameter	Symbol	Value	Unit
Vehicle mass	m_{car}	1800	kg
Gravitational acceleration	g	9.81	$m\cdot s^{-2}$
Car rolling resistance coefficient	f	0.012	_
Aerodynamic drag coefficient	C_D	0.32	_
Vehicle frontal area	A_f	2.3	m^2
Rotational mass coefficient	δ	1.1	_
Transmission efficiency	η	0.96	_
Electric conversion efficiency	η_E	0.95	_
Slope angle	α	0	rad

Data availability

Data will be made available on request.

References

[1] M. Shahjalal, T. Shams, M.E. Islam, et al., A review of thermal management for Li-ion batteries: prospects, challenges, and issues, J. Energy Storage 39 (2021) 102518.

[2] A.B. Padalkar, M.B. Chaudhari, A.B. Padalkar, et al., Impact of cooling on battery cycle life based on direct current internal resistance and machine learning model prediction, Sustain. Energy Technol. Asses. 82 (2025) 104543.

[3] S. Kumar, R. Akula, C. Balaji, An inverse methodology to estimate the thermal properties and heat generation of a Li-ion battery, Appl. Therm. Eng. 236 (2024) 121752.

[4] Q. Wang, P. Ping, J. Sun, Experimental and numerical study on specific heat capacity of lithium-ion battery, J. Energy Storage 95 (2024) 112534.

[5] K. Maher, A. Boumaiza, R. Amin, Understanding the heat generation mechanisms and the interplay between joule heat and entropy effects as a function of state of charge in lithium-ion batteries, J. Power Sour. 623 (2024) 235504.

[6] J. Shi, H. Zhang, H. Yu, et al., Experimental determinations of thermophysical parameters for lithium-ion batteries: a systematic review, ETransportation 20 (2024) 100321.

[7] A. Loges, S. Herberger, P. Seegert, et al., A study on specific heat capacities of Li-ion cell components and their influence on thermal management, J. Power Sour. 336 (2016) 341–350.

[8] T.S. Bryden, B. Dimitrov, G. Hilton, et al., Methodology to determine the heat capacity of lithium-ion cells, J. Power Sour. 395 (2018) 369–378.

[9] M. Faber, O. Buitkamp, S. Ritz, et al., A method to determine the specific heat capacity of lithium-ion battery cells using thermal insulation, J. Power Sour. 583 (2023) 233499.
[10] H.Y. Zhang, L. Sheng, L. Su, Test method and device for specific heat of power battery (CN 108732204A), 2018 (05–02).
[11] L. Sheng, L. Su, H. Zhang, et al., An improved calorimetric method for characterizations of the specific heat and the heat generation rate in a prismatic lithium ion battery cell, Energy Convers. Manage. 180 (2019) 724–732.
[12] K.A. Murashko, A.V. Mityakov, J. Pyrhönen, et al., Thermal parameters determination of battery cells by local heat flux measurements, J. Power Sour. 271 (2014) 48–54.
[13] M. Auch, T. Kuthada, A. Wagner, Simple experimental method to determine the specific heat capacity of cylindrical lithium-ion-battery cells, Appl. Therm. Eng. 234 (2023) 121212.
[14] V.K. Chauhan, J. Bhattacharya, Error estimation of Bernardi heat evaluation of Li-ion cells under drive cycle operation, Appl. Therm. Eng. 254 (2024) 123870.
[15] X. Xu, H. Zhang, S. Liu, et al., Surrogate models for lithium-ion battery heat generation based on orthogonal experiments by eliminating external wire connection effect, Appl. Therm. Eng. 213 (2022) 118655.
[16] P. Jindal, R. Katiyar, J. Bhattacharya, Evaluation of accuracy for Bernardi equation in estimating heat generation rate for continuous and pulse-discharge protocols in LFP and NMC based Li-ion batteries, Appl. Therm. Eng. 201 (2022) 117794.
[17] Y. Hu, S.Y. Choe, T.R. Garrick, Measurement of heat generation rate and heat sources of pouch type Li-ion cells, Appl. Therm. Eng. 189 (2021) 116709.
[18] J. Ding, K. Liu, C. Xu, et al., Accelerating rate calorimetry: history, state of the art and perspectives, Chem. Thermodynamics and Thermal Anal. 18 (2025) 100182.
[19] X. He, C. Zhao, Z. Hu, et al., Heat transfer effects on accelerating rate calorimetry of the thermal runaway of lithium-ion batteries, Process. Saf. Environ. Prot. 162 (2022) 684–693.
[20] Y. Yang, D. Raymand, D. Brandell, A cost-effective alternative to accelerating rate calorimetry: analyzing thermal runaways of lithium-ion batteries through thermocouples, J. Power Sour. 612 (2024) 234807.
[21] Q. Wu, H. Zhang, J. Li, Measurement of specific heat capacity and heat generation rate of lithium-ion batteries using a calibration calorimetry method, Automot. Eng. 42 (1) (2020) 59–65.
[22] L. Sheng, Z. Zhang, L. Su, et al., A calibration calorimetry method to investigate the thermal characteristics of a cylindrical lithium-ion battery, Int. J. Therm. Sci. 165 (2021) 106891.
[23] Y. Kimura, K. Utsumi, H. Tohmyoh, Experimental relationship between the Seebeck and Peltier effects in thermoelectric modules based on Fe and Al metals, Appl. Therm. Eng. 255 (2024) 124009.
[24] T. Matsuoka, T. Nishihara, D. Matsugi, et al., Necessary condition for measurement of heat flux sensor using a thermoelectric module, Fire Saf. J. 125 (2021) 103427.
[25] Q. Liu, T. Huang, X. Chen, et al., Measurement of non-equilibrium characteristics of thermoelectric materials, J. Mater. Res. Technol. 28 (2024) 2740–2751.
[26] W. Yuan, H. Zhang, W. He, et al., Self-calibrated calorimetry to minimize the measurement uncertainty of the specific heat and heat generation rate for prismatic batteries, Int. J. Heat Mass Transf. 247 (2025) 127172.
[27] B. Keyhani-Asl A, N. Perera, J. Lahr, et al., Innovative hybrid battery thermal management system incorporating copper foam porous fins and layers with phase change material and liquid cooling, Appl. Therm. Eng. 268 (2025) 125848.
[28] J. Cen, Z. Li, F. Jiang, Experimental investigation on using the electric vehicle air conditioning system for lithium-ion battery thermal management, Energy Sustain. Dev. 45 (2018) 88–95.
[29] E. Tardy, P.X. Thivel, F. Druart, et al., Internal temperature distribution in lithium-ion battery cell and module based on a 3D electrothermal model: an investigation of real geometry, entropy change and thermal process, J. Energy Storage 64 (2023) 107090.
[30] W. Zhou, L. Zhang, G. Wang, et al., Impacts of urban expansion on air temperature and humidity during 2022 mega-heatwave over the Yangtze River Delta, China, Sci. Total Environ. 951 (2024) 175804.
[31] Y. Rezgui, M. Guemini, A. Tighezza, Realistic heat generation modeling and experimental validation for lithium-ion battery cells and modules, J. Energy Storage 138 (2025) 118769.
[32] J. Jahanpanah, P. Soleymani, N. Karimi, et al., Transient cooling of a lithium-ion battery module during high-performance driving cycles using distributed pipes-a numerical investigation, J. Energy Storage 74 (2023) 109278.
[33] Z. Cheng, X. Ji, D.G. Cahill, Battery absorbs heat during charging uncovered by ultra-sensitive thermometry, J. Power Sour. 518 (2022) 230762.
[34] S. Liu, H. Zhang, X. Xu, A study on the transient heat generation rate of lithium-ion battery based on full matrix orthogonal experimental design with mixed levels, J. Energy Storage 36 (2021) 102446.
[35] X. Li, D. Zhao, Y. Wang, et al., Investigation on the heat generation and heat sources of cylindrical NCM811 lithium-ion batteries, Appl. Therm. Eng. 221 (2023) 119852.
[36] X. Li, X. Chang, Y. Feng, et al., Investigation on the heat generation and heat sources of cylindrical NCM811 lithium-ion batteries, Appl. Therm. Eng. 241 (2024) 122403.
[37] Keysight Technologies, Data Acquisition System Product Fact Sheet, 5992-3177, 2023. (Available online from the manufacturer).
[38] J.H. Shi, H.Y. Zhang, H. Yu, et al., Experimental determination of heat generation rates of lithium-ion batteries by thermal protection method, SCIENCE CHINA Technol. Sci. 67 (12) (2024) 3647–3658.
[39] C. Wu, L. Wu, C. Qiu, et al., Experimental and numerical studies on lithium-ion battery heat generation behaviors, Energy Rep. 9 (2023) 5064–5074.